

BACKGROUND MODEL FOR THE LOW-ENERGY TELESCOPE OF *INSIGHT-HXMT*

Jin-Yuan Liao¹, Shu Zhang¹, Yong Chen¹, Juan Zhang¹, Jing Jin¹, Zhi Chang¹, Yu-Peng Chen¹,
Ming-Yu Ge¹, Cheng-Cheng Guo^{1,2}, Gang Li¹, Xiao-Bo Li¹, Fang-Jun Lu¹, Xue-Feng Lu¹,
Jian-Yin Nie¹, Li-Ming Song¹, Yan-Ji Yang¹, Yuan You^{1,2}, Hai-Sheng Zhao¹,
Shuang-Nan Zhang^{1,2,3}

ABSTRACT

With more than 150 blank sky observations at high Galactic latitude, we make a systematic study to the background of the Low Energy Telescope (LE) of the *Hard X-ray Modulation Telescope* (dubbed as *Insight-HXMT*). Both the on-ground simulation and the in-orbit observation indicate that the background spectrum mainly has two components. One is the particle background that dominates above 7 keV and its spectral shape is consistent in every geographical locations. Another is the diffuse X-ray background that dominates below 7 keV and has a stable spectrum less dependent of the sky region. The particle background spectral shape can be obtained from the blind detector data of all the blank sky observations, and the particle background intensity can be measured by the blind detector at 10–12.5 keV. The diffuse X-ray background in the high Galactic latitude can also be obtained from the blank sky spectra after subtracting the particle background. Based on these characteristics, we develop the background model for both the spectrum and the light curve. The systematic error for the background spectrum is investigated with different exposures (T_{exp}). For the spectrum with $T_{\text{exp}} = 1$ ks, the average systematic errors in 1–7 keV and 1–10 keV are 4.2% and 3.7%, respectively. We also perform the systematic error analyses of the background light curves with different energy bands and time bins. The results show that the systematic errors for the light curves with different time bins are $< 8\%$ in 1–10 keV.

Subject headings: instrumentation: detectors — space vehicles: instruments — methods: data analysis — X-rays: general

¹Key Laboratory of Particle Astrophysics, Institute of High Energy Physics, Chinese Academy of Sciences, Beijing 100049, China; liaojinyuan@ihep.ac.cn

²University of Chinese Academy of Sciences, Chinese Academy of Sciences, Beijing 100049, China

³National Astronomical Observatories, Chinese Academy of Sciences, Beijing, 100012, China

1. INTRODUCTION

The Low Energy X-ray Telescope (LE) is one of the three main payloads of the *Hard X-Ray Modulation Telescope* (dubbed as *Insight-HXMT*) that has been operating in orbit since June 15th, 2017 (Zhang et al. 2020). LE is composed of Swept Charge Devices (SCDs) that are sensitive in 0.7–13 keV with a total geometrical area of 384 cm² (Chen et al. 2020). By using LE and the other two main payloads together, i.e., the Medium Energy X-ray Telescope (5–30 keV, Cao et al. 2020) and the High Energy X-ray Telescope (20–250 keV, Liu et al. 2020), *Insight-HXMT* can be used for wide-band spectral and temporal analyses. The main structure of *Insight-HXMT* and the LE detector modules are shown in Figure 1. As described in Chen et al. (2020), LE is a collimated type of telescope that consists of three detector boxes with orientation of the field of views (FOVs) offset by 60° (Figure 2). Each detector box contains 20 SCD type of detectors with the small FOVs (1°.6 × 6°), six detectors with the large FOVs (4° × 6°), one blind detector with a small FOV collimator, and one blind detector with a large FOV collimator that is accompanied by a Fe⁵⁵ radioisotope to monitor the possible change of the energy response.

Insight-HXMT operates on a quasi-circular low-earth orbit with an altitude of ~ 550 km and an inclination of $\sim 43^\circ$. There are various particles that can interact with the satellite platform and the payloads, e.g., the cosmic-ray protons and electrons (Alcaraz et al. 2000a, 2000b), the gamma-rays and neutrons reflected from the earth (Imhof et al. 1976; Armstrong et al. 1973), and the cosmic X-ray background (CXB, Gehrels 1992, Abdo et al. 2010). The complexity of the space environment is also revealed by long-term observations of the particle monitor onboard *Insight-HXMT* (Lu et al. 2019; Liao et al. 2020). According to the on-ground simulation (Li et al. 2015), the LE background can be roughly divided into two parts, i.e., the particle background that is dominant in high energy band (> 7 keV) and the diffuse X-ray background that is dominant in low energy band (< 7 keV).

In this paper, we focus on the particle background and the diffuse X-ray background in high Galactic latitude ($|b| < 10^\circ$) and the region far from the Galactic center ($90^\circ < l < 270^\circ$). The diffuse X-ray background in the Galactic center is strong and complex (Snowden et al. 1997). LE has relatively large FOVs, thus the diffuse X-ray background of LE in the Galactic center needs to be considered seriously. Currently, the Galactic diffuse background is estimated from *Insight-HXMT* Galactic plane scanning survey, for which the details will be reported in a forthcoming paper.

This paper is organized as follows. The data reduction of *Insight-HXMT*/LE is shown in Section 2. In Section 3, we show the main observational characteristics of the background of *Insight-HXMT*/LE. In Section 4, we describe the method to estimate the LE background. The model test and discussion of the background estimation are shown in Section 5, respectively. The summary is given in Sections 6.

2. DATA REDUCTION

2.1. Preliminary data reduction

The preliminary data reduction is performed with the *Insight-HXMT* data analysis software HXHTDAS v2.1. For every blank sky observation, three tools are run before the spectra and the light curves are generated, as shown in the follows.

- `lepical`: PI transformation to obtain the energy-calibrated events..
- `lerecon`: Event reconstruction to select the non-split events.
- `legtigen`: Good Time Interval (GTI) selection to obtain the data within the specified parameter range.

In LE GTI selection, the earth elevations (ELV) are selected as $> 10^\circ$ to avoid the earth occultation of the blank sky. As the LE backgrounds are usually unstable due to the complex space environment near the South Atlantic Anomaly (SAA), the time since the last passage from SAA (T_SAA) and the time to the next SAA passage (TN_SAA) are both set to > 300 s. The geomagnetic cut-off rigidity (COR) is anti-correlated to particle flux and the LE background level. Since the LE background is high but stable in the low COR region, COR is ignored in the LE GTI selection. When a large number of the visible light or low-energy charged particles enter the collimator, the detectors will be saturated, thus `DYE_ELV` is generally chosen as $> 20^\circ$ in the regular pointing observations. However, there are still some anomalous peaks in the light curve when the satellite passes through the precipitating particle areas near the equator and the high latitude regions, even if `DYE_ELV` is $> 60^\circ$. Therefore, `DYE_ELV` is also ignored in the LE GTI selection and a more reliable and efficient method is added to the LE GTI selection instead.

2.2. GTI prior selection

For a pointing observation with the normal detector state, the variabilities of the source and the particle background are similar among the detectors with the small and large FOVs. Moreover, the diffuse X-ray backgrounds are proportional to the FOVs and can be considered as a constant for each detector. Therefore, the difference between the light curve of the large and small FOV detectors is almost constant since they are caused by the different contribution of the diffuse X-ray backgrounds. Figure 3 shows an example of a LE light curve of a blank sky observation, where several flares are obvious in the light curves of both the large and small FOVs. Compared to the low energy band (1–7 keV), the flares are much more significant in the high energy band (7–13 keV).

As the flares are proportional to the FOVs and have a typical duration of several hundreds seconds, which is very different from the diffuse X-ray backgrounds, we speculate that the flares may be the result of a large number of low-energy charged particles entering the collimator. Such a speculation is further supported by the on-ground Geant4 simulation. As shown in Figure 4, the difference of the two light curves in 7–13 keV remains constant for most of the time, hence it serves as a prior GTI selection criterion for removing the flares events, which is described in what follows in details.

- Obtain the difference of the light curves of the large and small FOV detectors.
- The time period with the difference remains constant for more than 100 s (to avoid accidents) is adopted as the GTI of *Insight-HXMT/LE*.

For the pointing observation, the GTI prior selection is made first, and then the regular GTI selection is performed to obtain the final GTI of *Insight-HXMT/LE*.

3. OBSERVATIONAL CHARACTERISTICS OF LE BACKGROUND

Figure 5 shows the spectra of a blank sky observation with the blind and small FOV detectors of *Insight-HXMT/LE*. Because an aluminum plate blocks the FOV of the collimator, the blind detector cannot receive the X-ray photons in the LE working band, thus the blind detector can be considered as the pure particle background spectrum estimator (shown with the red color in Figure 5). The background spectra of the small FOV detectors above 7 keV are consistent with these of the blind detectors, and the diffuse X-ray backgrounds are dominant below 7 keV (shown with the blue color in Figure 5). Therefore, the particle background spectra of the small FOV detectors can be indicated with the spectra of the blind detectors, and the difference between the spectra of the blind and small FOV detectors is the diffuse X-ray background detected by *Insight-HXMT/LE*. An obvious geographical modulation shows up in the light curve (Figure 6), due to the anti-correlation between the particle background and COR (Figure 7). Such a phenomenon is indicated in the on-ground simulation (Li et al. 2015) and observed by other telescopes (e.g., *Suzaku*, Fukazawa et al. 2009).

4. MODELING OF LE PARTICLE BACKGROUND

4.1. Spectrum of LE Particle Background

The background of LE is mainly composed of several prompt background components. In high-energy band (> 7 keV), the particle background is dominant with intensity varying with the

geographical locations; and in low-energy band (< 7 keV), the diffuse X-ray background is dominant with intensity remaining constant during a pointing observation.

Based on more than 150 observations of the blank sky in high Galactic latitude, we find that the spectral shapes of the particle backgrounds are stable in different COR ranges for both the blind and small FOV detectors (Figure 8–9). Accordingly, the estimation of the background spectra is highly be simplified: the spectrum of the particle background is measured first and then the background model is completed by adjusting the intensity. All we need to do is to find the best indicator of the background intensity. A variety of parameter combinations are investigated (Figure 10), which includes but are not limited to the signals over the upper threshold (with and without the splitting events), the integrated count rate of the blind detector in high-energy band (with and without the splitting events). By investigating the the correlation between different parameters, we find that the integrated count rate (10–12.5 keV) is mostly correlated to the background intensity (Figure 10c). In order to reduce the statistical errors, both the blind detectors with small and large FOVs are used, i.e., the integrated count rate (10–12.5 keV) of the small and large FOVs detectors are used to indicate the background intensity. The details are shown as follows.

a. Analyze every blank sky observation and merge all the spectra of the blind detectors, used as the spectral shape of the background of the small FOV detectors: $S_{\text{Mod}}(c|\text{SD})$

b. Analyze every blank sky observation and obtain the count rate in 10–12.5 keV (ΔE_h) of both the detectors with small and large FOVs: $R_{\text{BS},i}(\Delta E_h|\text{SD})$ and $R_{\text{BS},i}(\Delta E_h|\text{BD})$, where BS denote the “Blank sky” and $i = 0, 1, \dots, n$.

c. Obtain the ratio of the count rate in 10–12.5 keV between the small and blind FOV detectors

$$f = \frac{\sum_{\text{All}} R_{\text{BS},i}(\Delta E_h|\text{SD})}{\sum_{\text{All}} R_{\text{BS},i}(\Delta E_h|\text{BD})}, \quad (1)$$

d. For a pointing observation, with the count rate of the blind FOV detector in 10–12.5 keV $R_{\text{Obs}}(10-12.5 \text{ keV}|\text{BD})$ and the ratio in step c, obtain the expected count rate of the particle background of the small FOV detector in 10–12.5 keV

$$R_{\text{Exp}}(\Delta E_h|\text{SD}) = R_{\text{Obs}}(\Delta E_h|\text{BD}) \cdot f, \quad (2)$$

e. Obtain the correction factor of the background intensity

$$F = \frac{R_{\text{Exp}}(\Delta E_h|\text{SD})}{R_{\text{Mod}}(\Delta E_h|\text{SD})}, \quad (3)$$

f. Make the correction

$$S_{\text{Est}}(c|\text{SD}) = F \cdot S_{\text{Mod}}(c|\text{SD}). \quad (4)$$

The whole calculation process of the background spectra can be described as

$$S_{\text{Est}}(c|\text{SD}) = \frac{R_{\text{OBS}}(\Delta E_{\text{h}}|\text{BD})}{R_{\text{Mod}}(\Delta E_{\text{h}}|\text{SD})} \frac{\sum_{\text{All}} R_{\text{BS},i}(\Delta E_{\text{h}}|\text{SD})}{\sum_{\text{All}} R_{\text{BS},i}(\Delta E_{\text{h}}|\text{BD})} S_{\text{Mod}}(c|\text{SD}). \quad (5)$$

4.2. Light Curve of LE Particle Background

The background model for light curve follows a procedure similar to that for energy spectrum and is shown in details in what follows.

- a. Obtain the observational light curve of the blind FOV detectors in 10–12.5 keV: $L_{\text{Obs}}(t; \Delta E_{\text{h}}|\text{BD})$.
- b. Obtain the expected background light curve of the small FOV detector in 10–12.5 keV

$$L_{\text{Exp}}(t; \Delta E_{\text{h}}|\text{SD}) = L_{\text{Obs}}(t; \Delta E_{\text{h}}|\text{BD})f, \quad (6)$$

- c. Based on the background characteristics that the spectral shape is consistent in any geographical locations, obtain the ratio of the expected background in the special energy band and 10–12.5 keV

$$\mathcal{R}(t; \Delta E) = \frac{S_{\text{Mod}}(\Delta E|\text{SD})}{S_{\text{Mod}}(\Delta E_{\text{h}}|\text{SD})}, \quad (7)$$

- d. Finally, the background light curve of the special energy band can be obtained by

$$\begin{aligned} L_{\text{Est}}(t; \Delta E|\text{SD}) &= L_{\text{Exp}}(t; \Delta E_{\text{h}}|\text{SD})\mathcal{R}(t; \Delta E) \\ &= L_{\text{Obs}}(t; \Delta E_{\text{h}}|\text{BD}) \frac{S_{\text{Mod}}(\Delta E|\text{SD})}{S_{\text{Mod}}(\Delta E_{\text{h}}|\text{SD})} f. \end{aligned} \quad (8)$$

In order to reduce the statistical error, the background light curve with $T_{\text{bin}} = 16$ s is produced first. In addition, both the on-ground simulation and the in-orbit observation indicate the time scale of the variability of the LE background is always very long (> 100 s). Thus the background light curve with shorter time bin can be obtained by interpolating the background light curve with $T_{\text{bin}} = 16$ s.

5. MODEL TEST AND DISCUSSION

5.1. Estimation of the Diffuse Background in High Galactic Latitude

The observations of 21 blank sky regions in high Galactic latitudes are used to test the background model. For the blank sky observations in high Galactic latitude, the diffuse X-ray background caused by the CXB in the low energy band dominates the LE background spectrum.

Therefore, in order to test the particle background model, the CXB spectra must be obtained first. For every blank sky, the particle background spectrum is obtained with the background model first and then subtracted from the observational spectrum, thus the observed CXB spectrum with *Insight-HXMT* is obtained (Figure 11). With the maximum likelihood estimation described in Liao et al. (2013), we obtain the intrinsic dispersion of the CXB count rates in 3–7 keV among the adopted blank sky regions is $4.0 \pm 0.7\%$ (Figure 12). As shown in Revnivtsev et al. (2003), CXB has a fluctuation of 7% per square degree, and with the LE small FOV $1^\circ.6 \times 6^\circ$, the expected fluctuation of the LE diffuse X-ray background is $\sim 2.3\%$. Therefore, the measured CXB fluctuation of LE is slightly larger than the theoretical expectation, which may be due to the systematic error of calibration and the unresolved sources in each blank sky. However, such a deviation is relatively small and insignificant. Moreover, the CXB spectra obtained by *Insight-HXMT* can be well matched by the CXB spectral model with parameters given by *RTXE/PCA* (Revnivtsev et al. 2003), which indicates that the particle background is reliable. In the following, the average of all the diffuse X-ray background spectra is considered as the diffuse X-ray background of a pointing observation to the high Galactic latitude region. We take the diffuse X-ray background in the high Galactic latitude as input and combine it with the particle background model to estimate the systematic error of the LE background modeling.

5.2. Test for the Background Spectra

In order to estimate the exposure dependence of the background spectrum model, all the blank sky observations are re-grouped into sub-observations with the same exposure (T_{exp}). Figure 13 shows the background spectral estimation of a blank sky observation with $T_{\text{exp}} = 1$ ks, 2 ks, 4 ks and 8 ks, respectively. An example of testing the background spectrum with $T_{\text{exp}} = 1$ ks is shown as follows.

- (1) Re-group all the blank sky observations into N sub-observations with $T_{\text{exp}} = 1$ ks and obtain their observational spectra $S_{i,\text{obs}}(c)$, where $i = 1, 2, \dots, N$.
- (2) Obtain the particle background spectra of these sub-observations with the particle background model.
- (3) Combine the particle background spectra and the diffuse X-ray background spectra to obtain the total background spectra $S_{i,\text{bkg}}(c)$, where $i = 1, 2, \dots, N$.
- (4) Compare $S_{\text{obs}}(c)$ and $S_{\text{bkg}}(c)$ to obtain the residuals $R(c) = S_{\text{obs}}(c) - S_{\text{bkg}}(c)$.
- (5) Calculate the mean value and intrinsic dispersion of $R(c)$ of each channel, i.e., R_m and D_{in} .

by solving the following equation

$$\sum_{i=1}^N \frac{(R_i - R_m)^2}{D_i^2} = N - 1, \quad (9)$$

where

$$D_i^2 = D_{\text{in}}^2 + \sigma_i^2, \quad (10)$$

$$R_m = \sum_{i=1}^N R_i \times w_i, \quad w_i = \frac{\frac{1}{D_i^2}}{\sum_{i=1}^N \frac{1}{D_i^2}}, \quad (11)$$

where R_i refers to the $R(c)$ of every observation, σ_i the statistic errors of R_i . R_m and D_{in} can be considered as the bias (B) and the systematic error (σ_{sys}) of the background estimation.

The same processes are also performed for $T_{\text{exp}} = 2, 4$ and 8 ks to obtain the systematic errors specific to these exposures. Figure 14 shows the distributions of the residuals resulted in the 200th channel of the background modeling with exposures 1 ks, 2 ks, 4 ks, and 8 ks, respectively. In each panel, the broadening of the histogram is the dispersion of the residuals caused by both the statistical error of the test data and the systematic error of the background model. As shown in Figure 15 and Table 1, the systematic error is 3.7% & 2.0% for $T_{\text{exp}} = 1$ & 8 ks in 1–10 keV, respectively. Because the systematic error is partly propagated from the statistical errors of the blind FOV detectors, which is reduced as the exposure increases, there is an anti-correlation between the systematic error and the exposure.

5.3. Test for the Background Light Curve

With the process described in Section 4.2, the background light curve can be obtained (Figure 16). All the blank sky observations are processed to obtain the light curves with four energy bands and eight time bins (Table 2). In the following, the background light curve in 1–10 keV with $T_{\text{bin}} = 1$ s is used as an example to shown the detailed processes of the model test.

(1) Merge all the blank sky observations into one observation with the energy band 1–10 keV and $T_{\text{bin}} = 1$ s and obtain the observational light curve (L_{obs}).

(2) Obtain the particle background light curve in 1–10 keV by the particle background model.

(3) Combine the particle background light curve and the diffuse X-ray background 1–10 keV in high Galactic latitude to obtain the total background light curve (L_{bkg}).

(4) Compare L_{obs} and L_{bkg} to obtain the residuals $R_L = L_{\text{obs}} - L_{\text{bkg}}$.

(5) Calculate systematic deviation and uncertainty with the method described in Section 5.2.

The above steps are also performed with the other parameters shown in Table 2. The distributions of the residuals with $T_{\text{bin}} = 16$ s in four energy bands are shown in Figure 17, and the detailed results of the systematic error analyses are also shown in Table 2.

6. SUMMARY

More than 150 blank sky observations are performed to study the background of *Insight-HXMT/LE*. We developed a new method to optimize the GTI selection, with which the abnormal flares can be removed in the preliminary data reduction for every blank sky observation. Both the in-orbit observation and the on-ground simulation indicate that the background of the small FOV detector of *Insight-HXMT/LE* is mainly composed of two parts; one is the particle background that is dominant in high-energy band (> 7 keV), and another is the diffuse X-ray background that is dominant in low-energy band (< 7 keV). With the blank sky observation, we find two important characteristics of the particle background, i.e., the spectral shape are consistent in every geographical location and the intensity can be indicated by the contemporary flux of the blind FOV detector in 10–12.5 keV. Based on these two characteristics, we developed the method to estimate the particle background of *Insight-HXMT/LE*. In addition, the diffuse X-ray background caused by the CXB is also obtained with the blank sky observation in the high Galactic latitude region. We investigated the exposure dependence of the systematic error induced from the current background modeling. For $T_{\text{exp}} > 1$ ks, the systematic error of the estimated background spectra is $\sim 3\%$ in 1–10 keV on average, which are partly attributed to the systematic error propagated from the statistical error of the blind detector during the background estimation. We also make the analysis to the light curve with different time bins. For the background light curves in 1–10 keV, the systematic errors are in general $< 8\%$. It is worth noting that the diffuse X-ray background in the Galactic center can be 2 times higher than that in the high Galactic region. Therefore, for the pointing observation of the Galactic center, the diffuse X-ray background is obtained from the sky map of the LE diffuse X-ray background, which will be described elsewhere in a forthcoming paper and thus not reported here.

This work made use of the data from the *Insight-HXMT* mission, a project funded by China National Space Administration (CNSA) and the Chinese Academy of Sciences (CAS). The authors thank supports from the National Program on Key Research and Development Project (Grant No. 2016YFA0400802 and 2016YFA0400801) and the National Natural Science Foundation of China under Grants No. U1838202 and U1838201.

REFERENCES

- Abdo, A. A., Ackermann, M., Ajello, M., et al. 2010, *PhRvL*, 104, 1101. DOI: 10.1103/PhysRevLett.104.101101
- Alcaraz, J., Alvisi, D., Alpat, B., et al. 2010, *PhLB*, 472, 215. DOI: 10.1016/S0370-2693(99)01427-6
- Alcaraz, J., Alpat, B., Ambrosi, G., et al. 2010, *PhLB*, 484, 10. DOI: 10.1016/S0370-2693(00)00588-8
- Armstrong, T. W., Chandler, K. C., Barish, J. 1973, *JGR*, 78, 2715. DOI: 10.1029/JA078i016p02715
- Cao, X. L., Jiang, W. C., Meng, B., et al. 2020, *SCPMA*, 63, 4: 249504 (2020). DOI: 10.1007/s11433-019-1506-1
- Chen, Y., Cui, W. W., Li, W., et al. 2020, *SCPMA*, 63, 4: 249505 (2020). DOI: 10.1007/s11433-019-1469-5
- Fukazawa, Y., Mizuno, T., Watanabe, S., et al. 2009, *PASJ*, 61, 17
- Gehrels, N. 1992, *NIMPA*, 313, 513. DOI: 10.1016/0168-9002(92)90832-O
- Imhof, W. L., Nakano, G. H., Reagan, J. B. 1976, *JGR*, 81, 2835. DOI: 10.1029/JA081i016p02835
- Li, G., Xie, F., Zhang, J., et al. 2015, *Progress in Astronomy*, 33, 233
- Liao, J. Y., Zhang, S. N., & Yao, Y.-S. 2013, *ApJ*, 774, 116. DOI: 10.1088/0004-637X/774/2/116
- Liao, J. Y., Zhang, S., Lu, X. F., et al. 2020, *JHEAp*, submitted
- Liu, C. Z., Zhang, Y. F., Li, X.-F., et al. 2020, *SCPMA*, 63, 4: 249503 (2020). DOI: 10.1007/s11433-019-1486-x
- Lu, X. F., Liu, C. Z., Zhang, S., et al. 2019, *JHEAp*. in press. arXiv:1911.01594
- Revnivtsev, M.; Gilfanov, M.; Sunyaev, R., et al. 2003, *A&A*, 411, 329. DOI: 10.1051/0004-6361:20031386
- Snowden, S. L., Egger, R., Freyberg, M. J., et al. 1997, *ApJ*, 485, 125. DOI: 10.1086/304399
- Zhang, S. N., Li, T. P., Lu, F. J., et al. 2020, *SCPMA*. 63, 4: 249502 (2020). DOI:10.1007/s11433-019-1432-6

Table 1. Systematic errors of the background spectra (1 – 10 keV) with different exposures

T_{exp}	1 ks	2 ks	4 ks	8 ks
$\sigma_{\text{sys}, 1-7 \text{ keV}}$	4.2%	3.8%	3.3%	2.8%
$\sigma_{\text{sys}, 1-10 \text{ keV}}$	3.7%	3.2%	2.7%	2.0%

Table 2. Systematic errors of the background light curves with different time bins

Energy Band	16 s	32 s	64 s	128 s
1 – 2 keV	6.2%	5.8%	5.9%	5.9%
2 – 6 keV	6.0%	6.2%	6.2%	6.2%
6 – 10 keV	12.7%	13.1%	13.3%	13.5%
1 – 10 keV	7.6%	7.6%	7.7%	7.8%

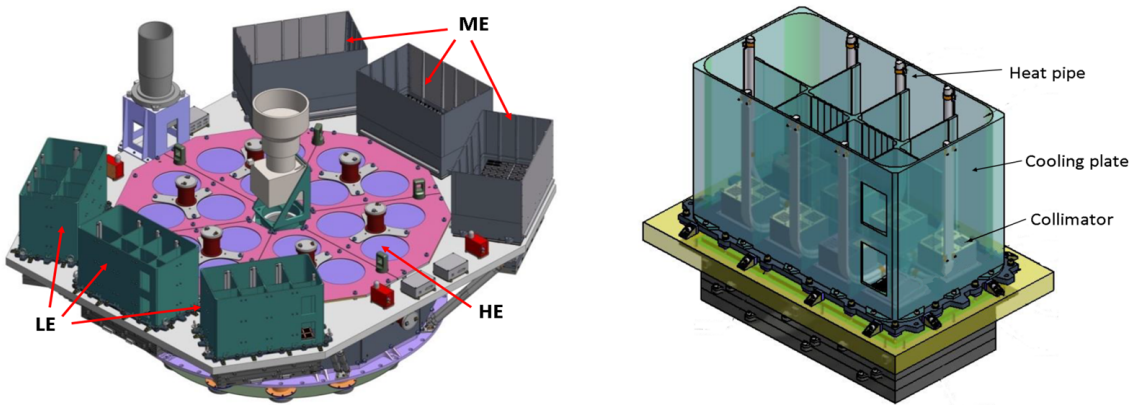


Fig. 1.— The main structure of *Insight-HXMT* and the LE detector modules.

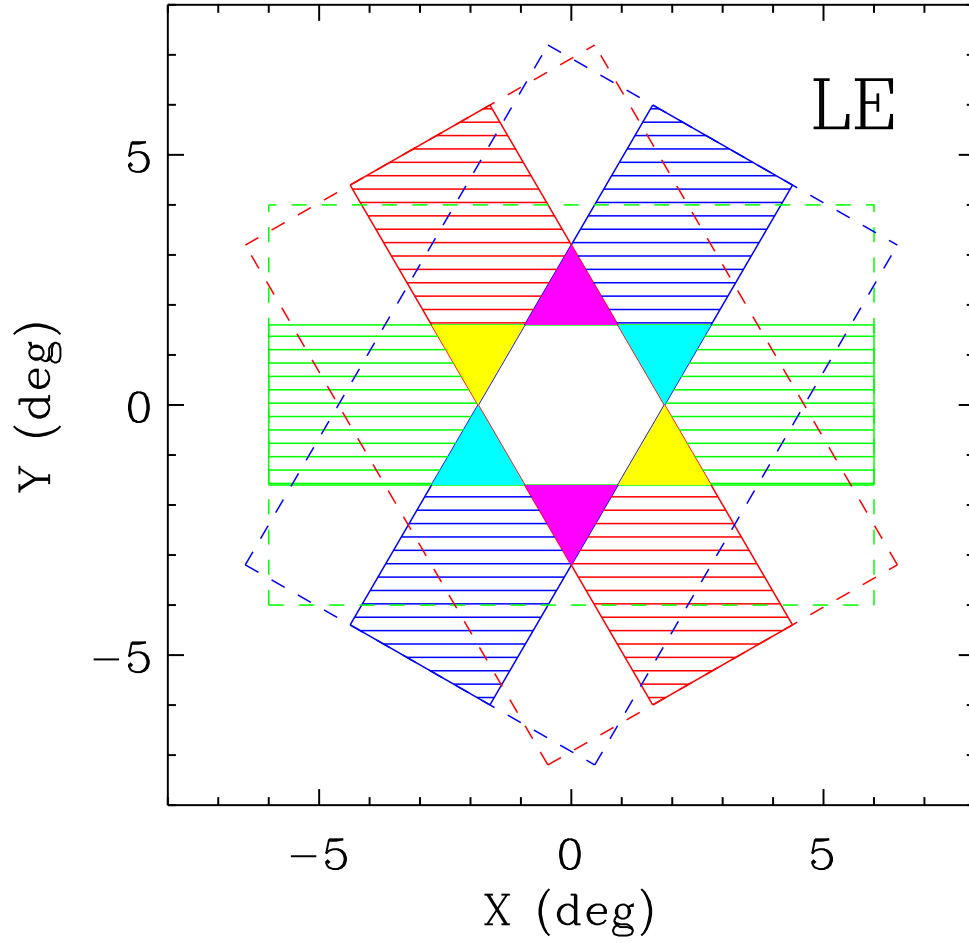


Fig. 2.— FOVs of the *Insight-HXMT/LE* detectors. Three rectangular shadows shown in red, blue and green are three small FOVs (FWHM: $1^\circ.6 \times 6^\circ$); and the three rectangles surrounded by the dashed lines are three large FOVs (FWHM: $4^\circ \times 6^\circ$).

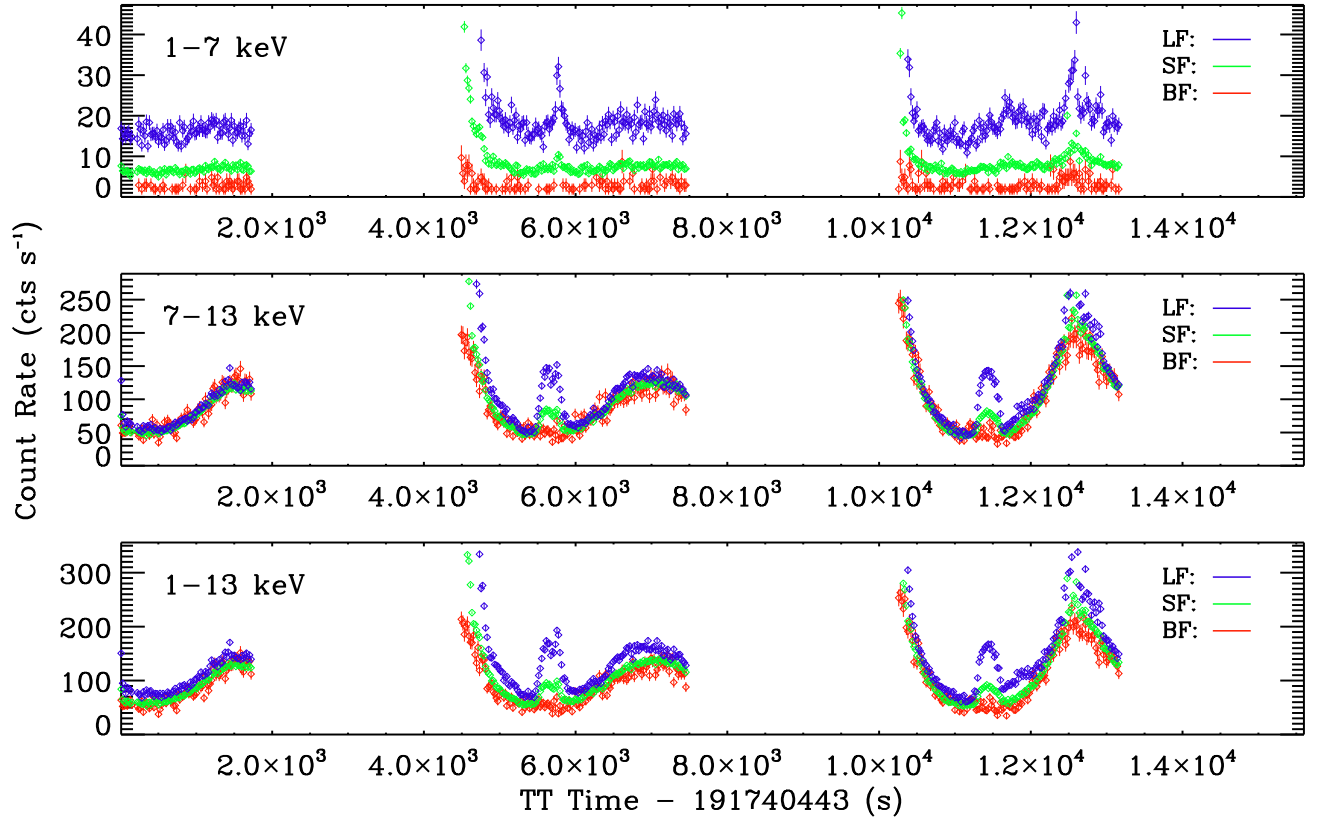


Fig. 3.— Light curves of a blank sky observation of *Insight-HXMT/LE* in 1–7 keV (top), 7–13 keV (middle), and 1–13 keV (bottom). In all three panels, the light curve of blind detector (L_{Blind}), small FOV detector (L_{Small}) and large FOV detector (L_{Large}) are shown in red, green and blue, respectively. Both the light curves of the blind and large FOV detectors are normalized by the ratio of the detector number with the small FOV detectors.

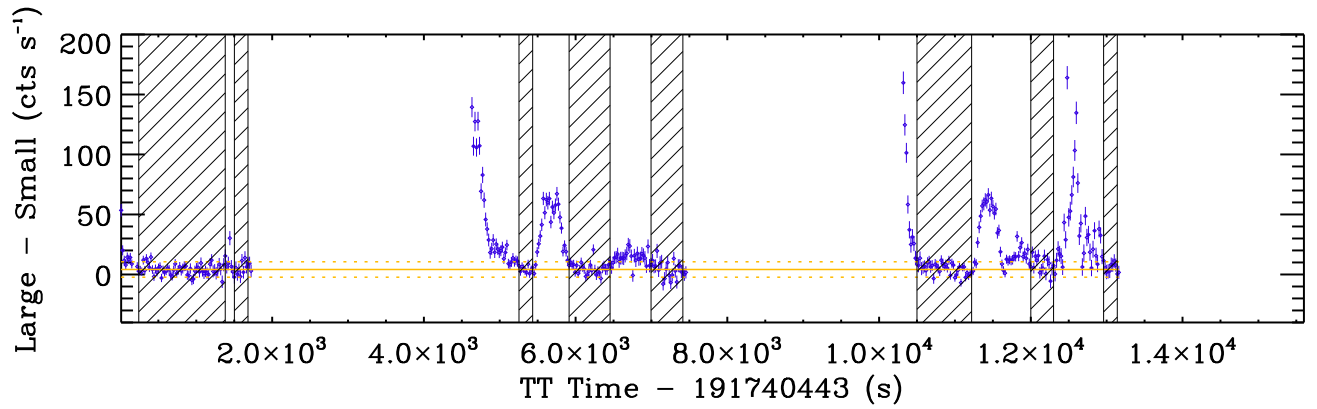


Fig. 4.— Difference between the light curves of large and small FOV detectors in 7–13 keV shown in Figure 3. The time after the GTI prior selection is marked with shadows.

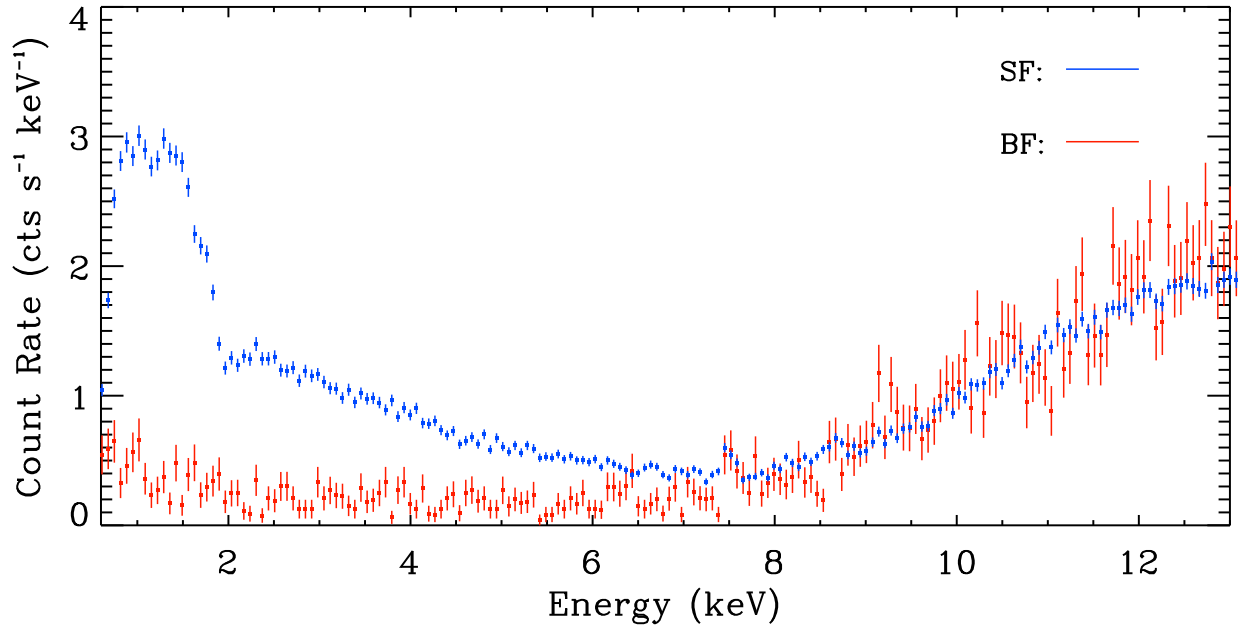


Fig. 5.— Spectra of a blank sky observed with the small FOV detector (blue) and the blind FOV detector (red).

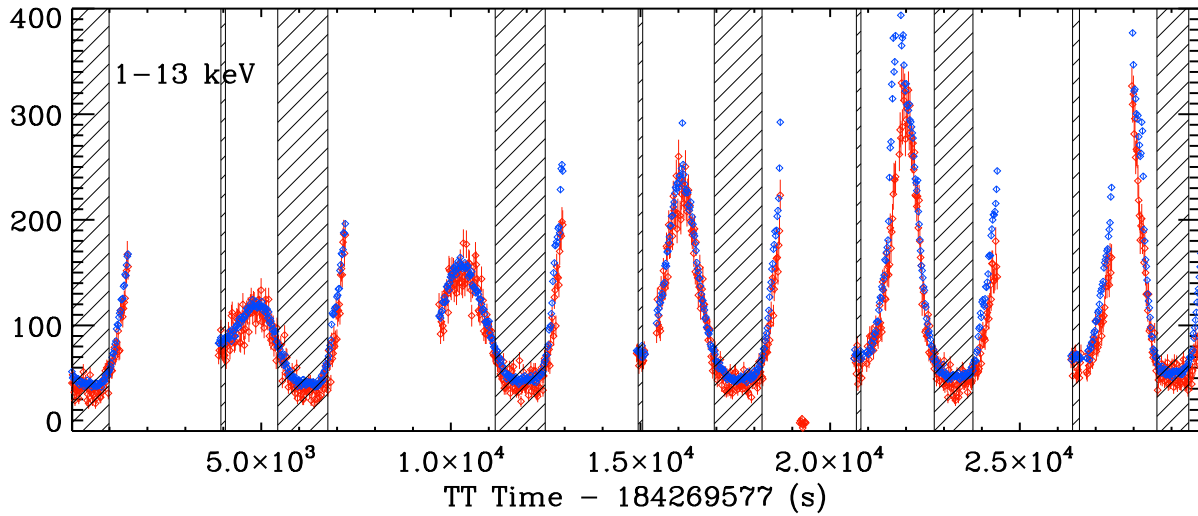


Fig. 6.— Light curves of a blank sky observed with the small FOV detector (blue) and the blind FOV detector (red). The final GTI is marked with shadows.

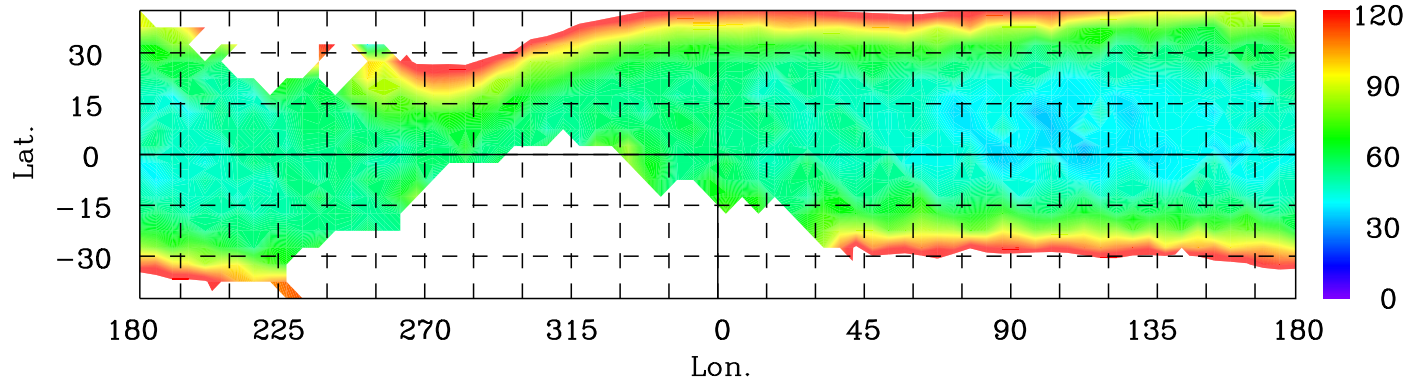


Fig. 7.— Geographical distribution of the background intensity (small FOV detector & 1–13 keV).

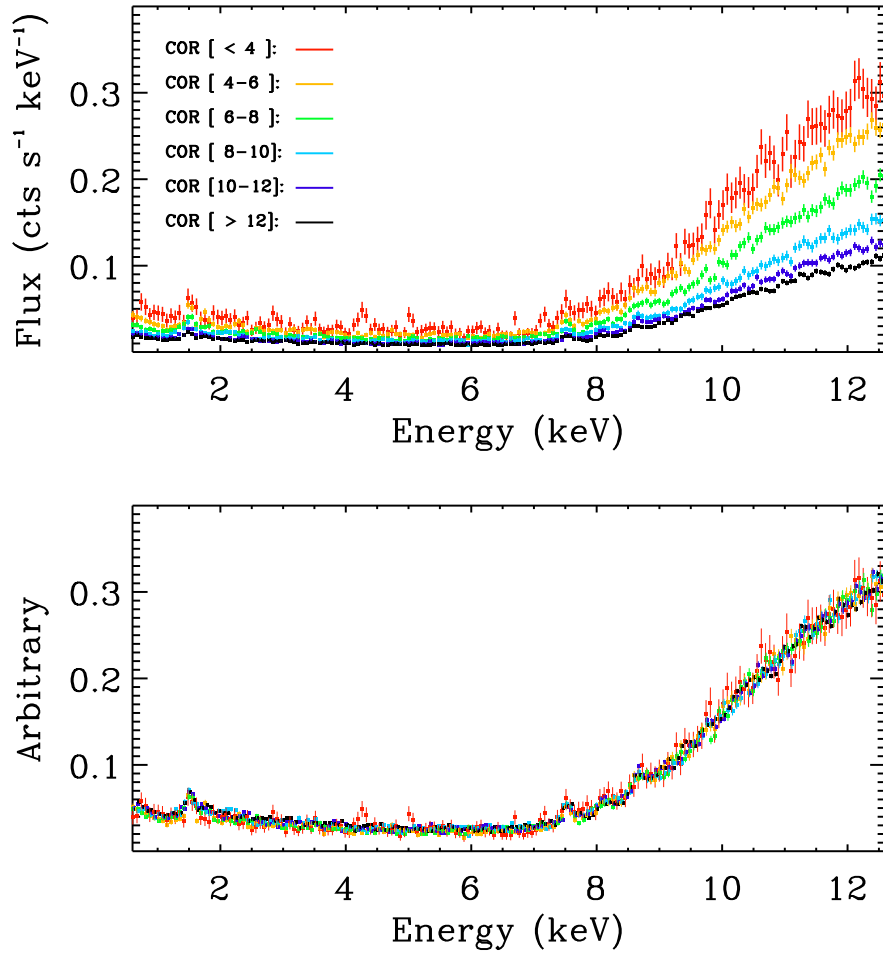


Fig. 8.— Top: Spectra of the blind FOV detector with different COR ranges. Bottom: normalized spectra of the top panel.

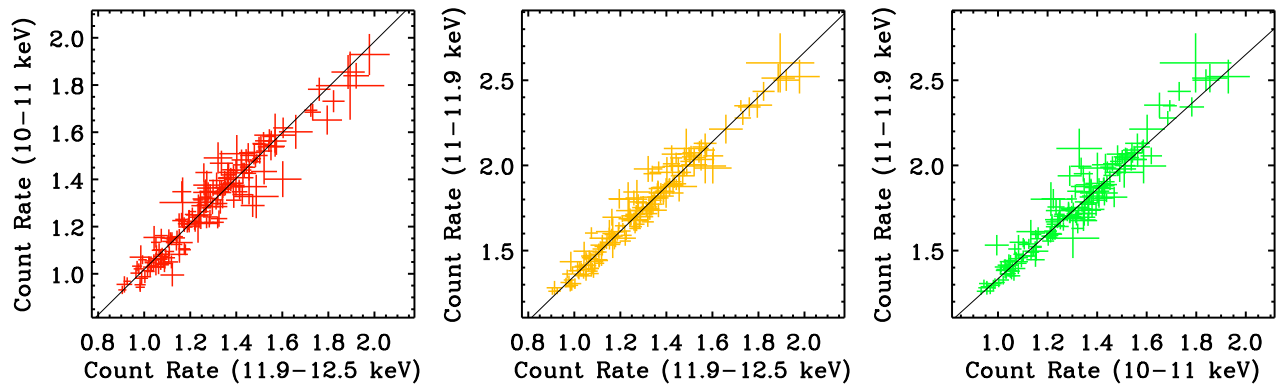


Fig. 9.— Correlations of the count rates in 10–11 keV, 11–11.9 keV and 11.9–12.5 keV. All the data are obtained from the blank sky observations with the small FOV detector.

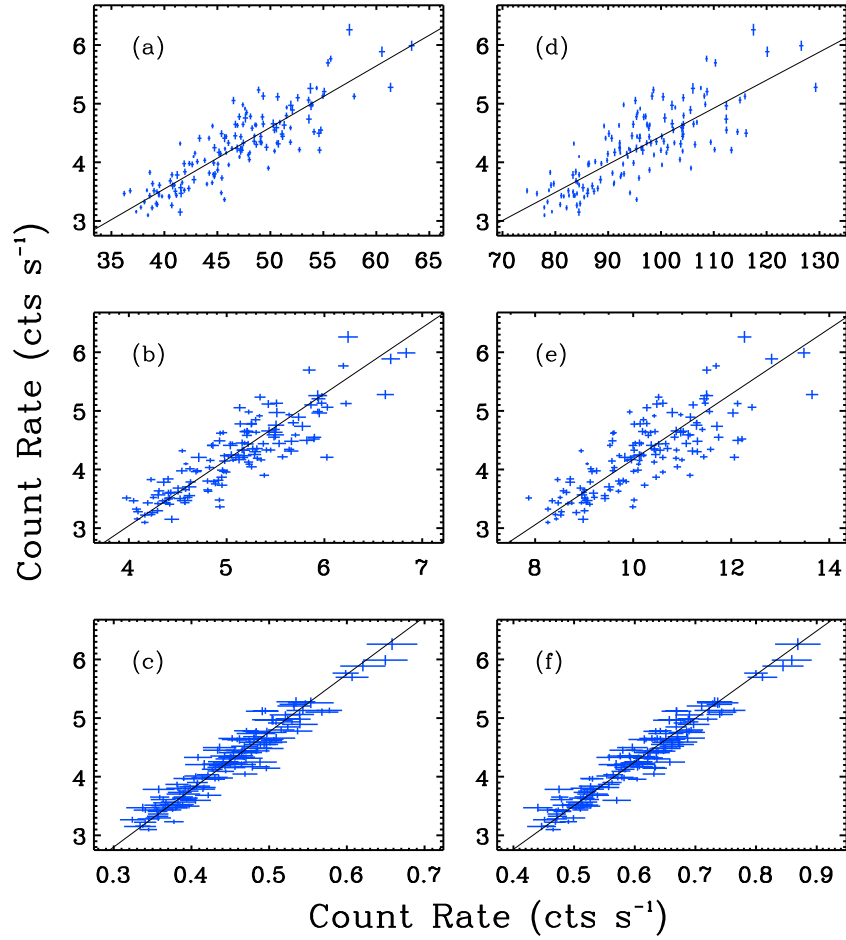


Fig. 10.— Correlation between the particle background of the small FOV detector and different variables. Panel (a): the count rate of the single event exceeding the upper threshold of the small FOV detector; Panel (b): the count rate of the single event exceeding the upper threshold of the blind FOV detector; Panel (c): the count rate of the single event in 10–12.5 keV of the blind FOV detector; Panel (d)–(f): the same as Panel (a)–(c) but also with the splitting events.

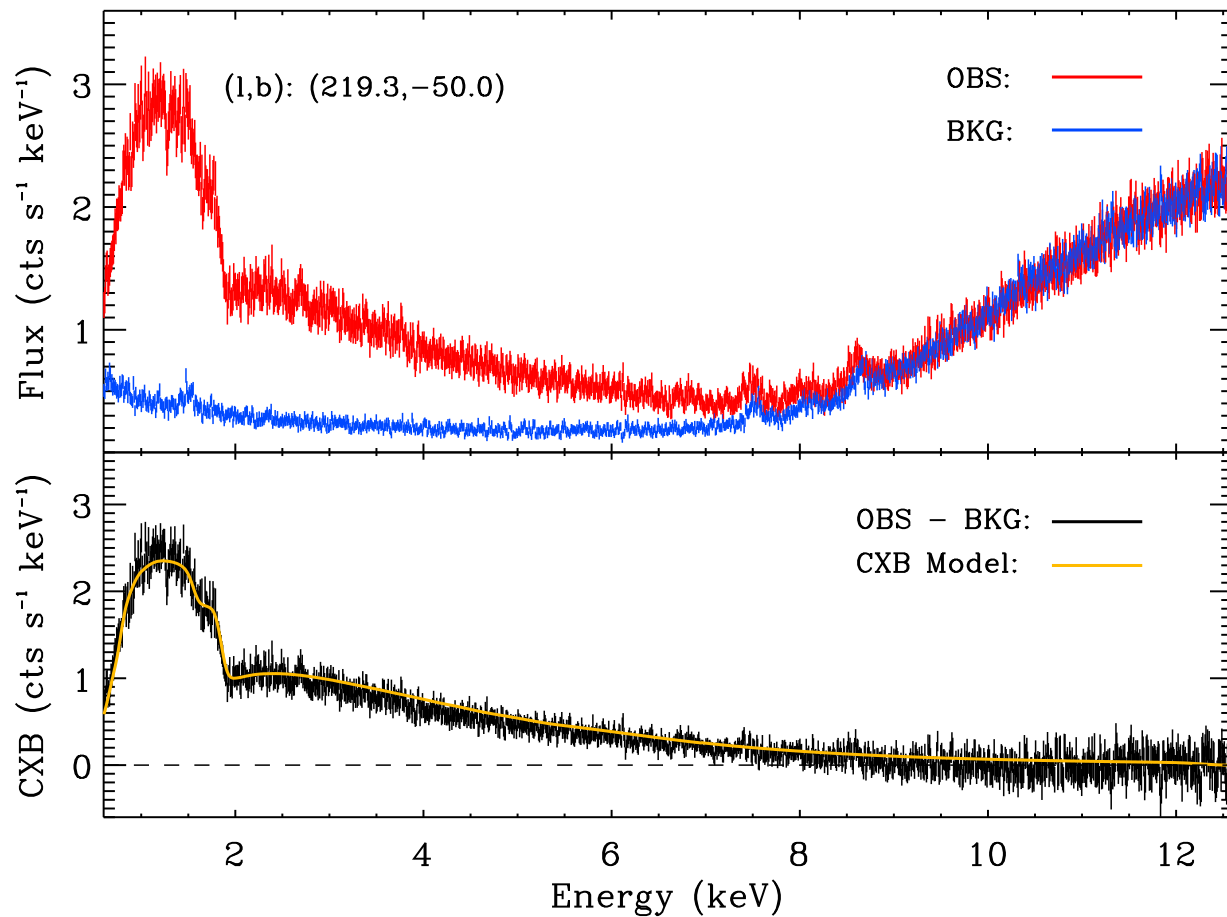


Fig. 11.— Top: spectrum of a blank sky observation (red) and the particle background spectrum (blue). Bottom: the CXB spectrum obtained from the blank sky observation by subtracting the particle background; The yellow curve is the model with the CXB spectral parameters (Revnivtsev et al. 2003) and the response of *Insight-HXMT/LE*.

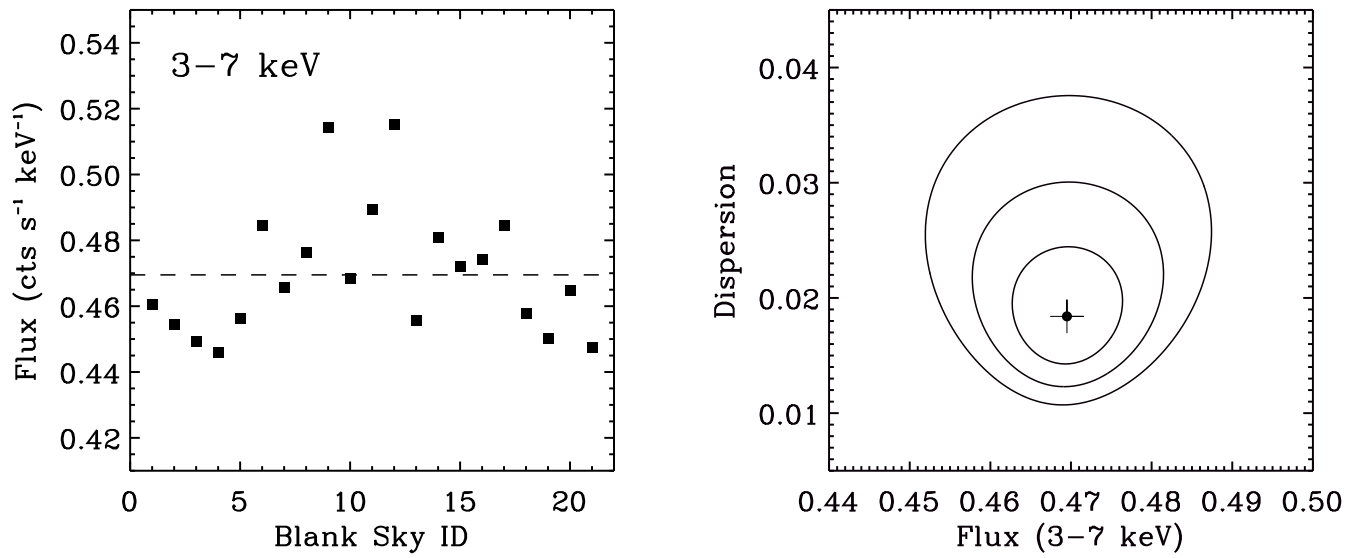


Fig. 12.— Left: the CXB count rates of 21 blank sky regions observed with *Insight-HXMT* in 3-7 keV. Right: the 2D posterior distribution of the mean value and the intrinsic dispersion of the CXB count rates obtained from the Bayesian analysis of the data in the left panel; the cross marks the maximum a posteriori estimates and the three contours from the inside out are the 1σ , 2σ and 3σ credible intervals, respectively.

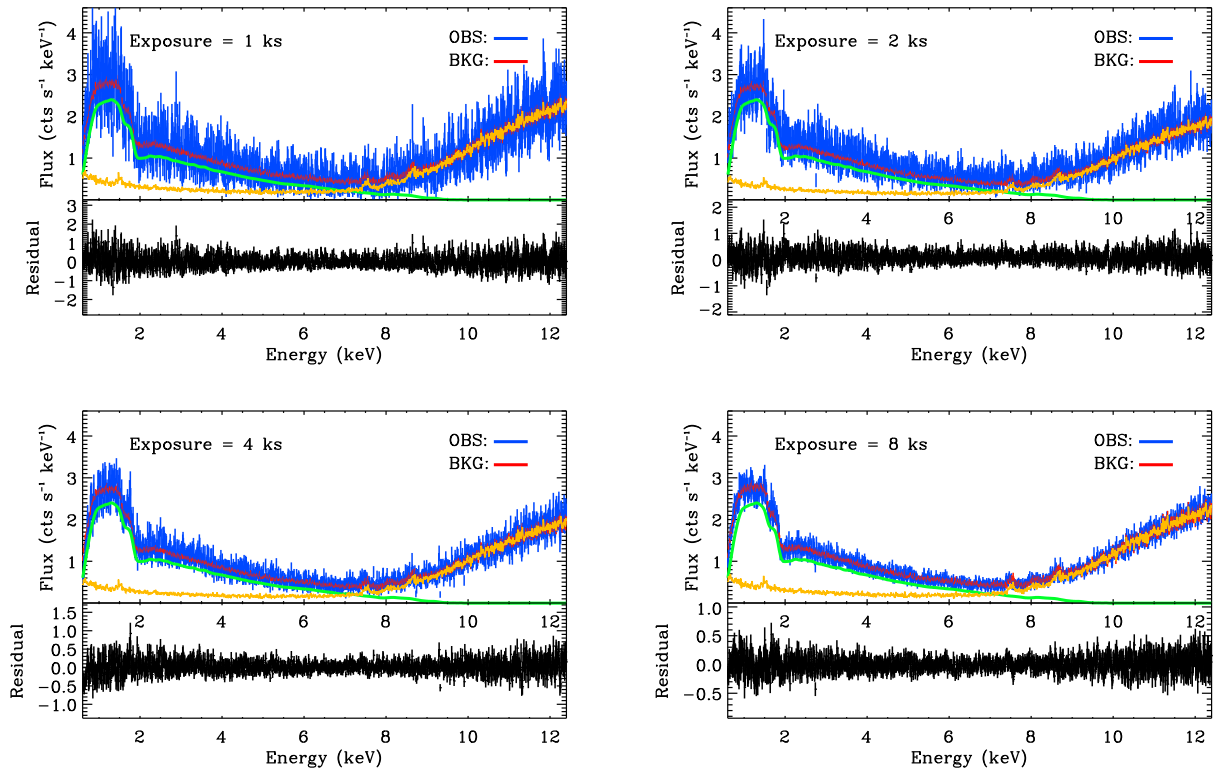


Fig. 13.— Background spectra test with the exposures 1 ks, 2 ks, 4 ks and 8 ks. Top of each panel: blue is the observed spectrum of a blank sky, red is the estimated background spectrum that is composed of the CXB spectrum (green) and the particle background spectrum (yellow). Bottom of each panel: residual of the background spectra estimation.

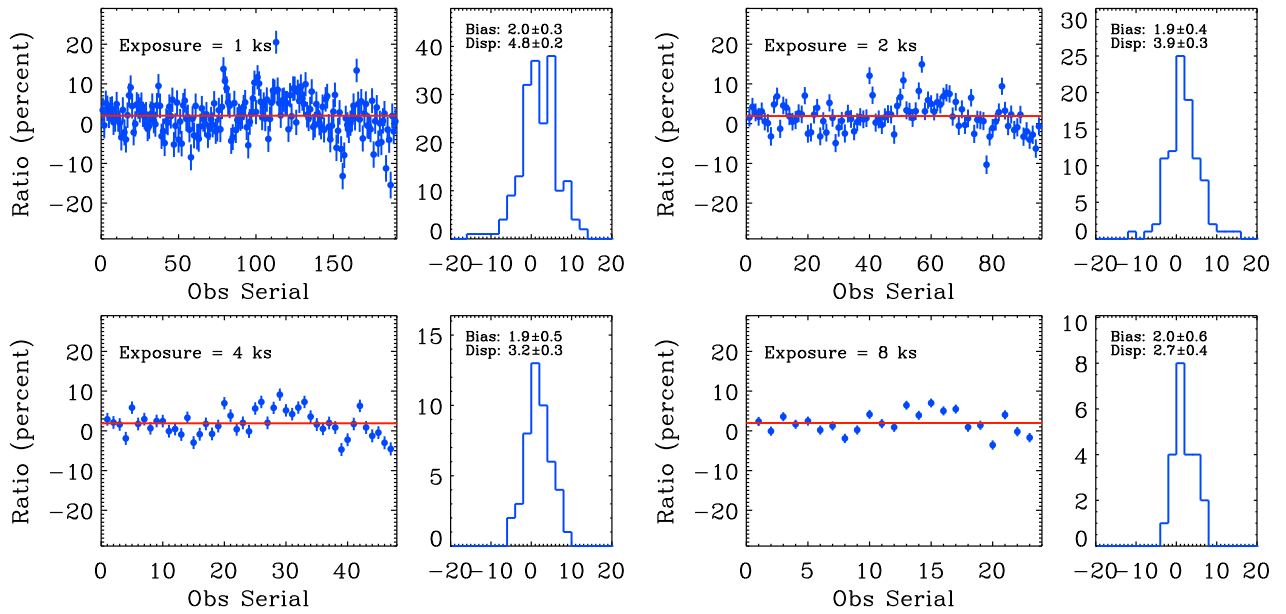


Fig. 14.— Distributions of the residuals in the background spectra estimation in the 200th channel with exposures 1 ks, 2 ks, 4 ks, and 8 ks. In each panel, the broadening of the histogram is the dispersion of the residuals that caused by both the statistical error of the test data and the systematic error of the background model.

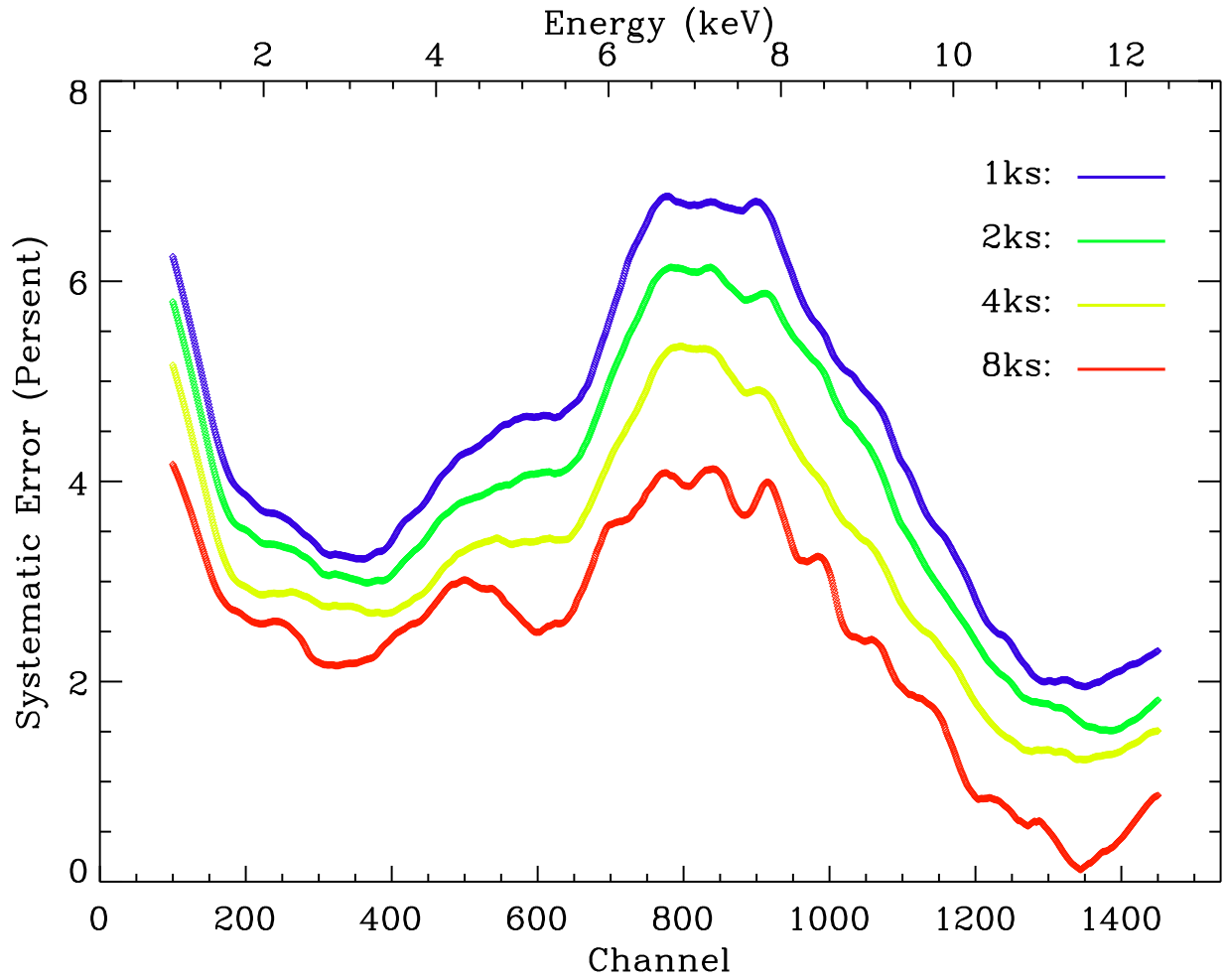


Fig. 15.— Systematic errors of the background spectra estimations in 1–12.4 keV with the exposures 1 ks, 2 ks 4 ks, and 8 ks.

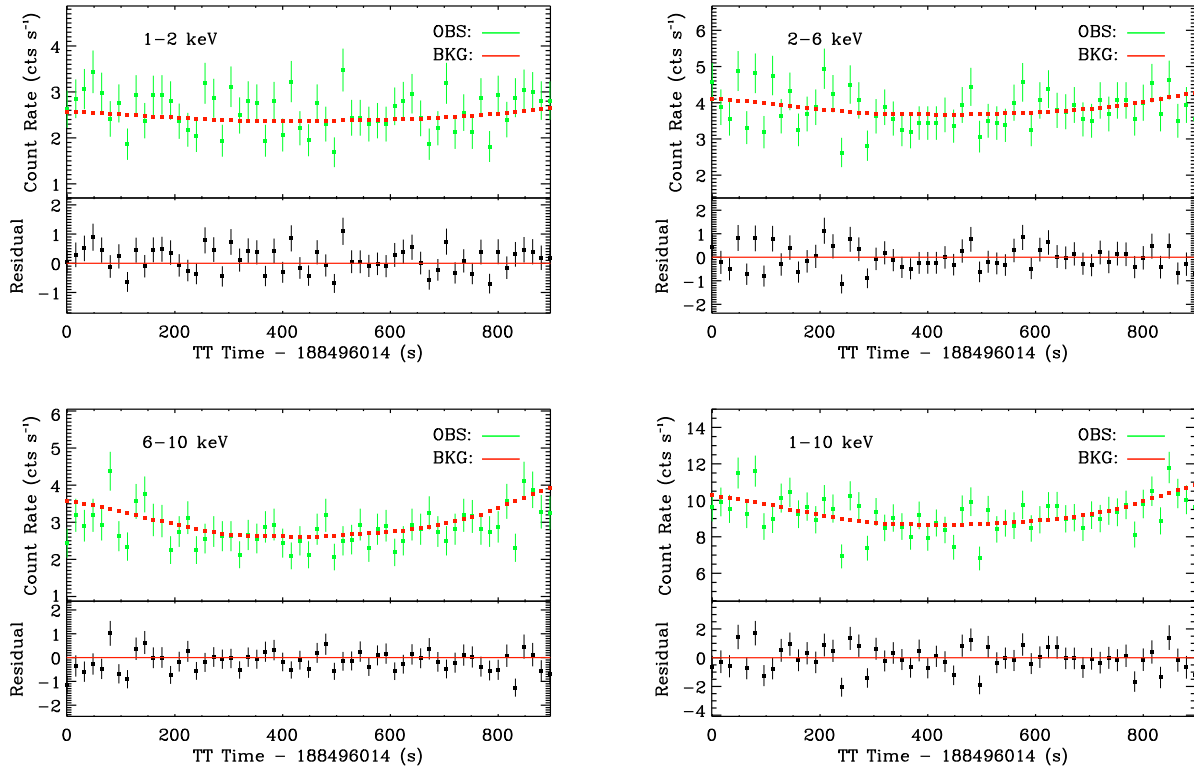


Fig. 16.— Test of the background light curve estimation in 1–2 keV, 2–6 keV, 6–10 keV and 1–10 keV with $T_{\text{bin}} = 16$ s. For each panel, the observed (green) and estimated (red) background light curves are shown in the top, and the residual is shown in the bottom.

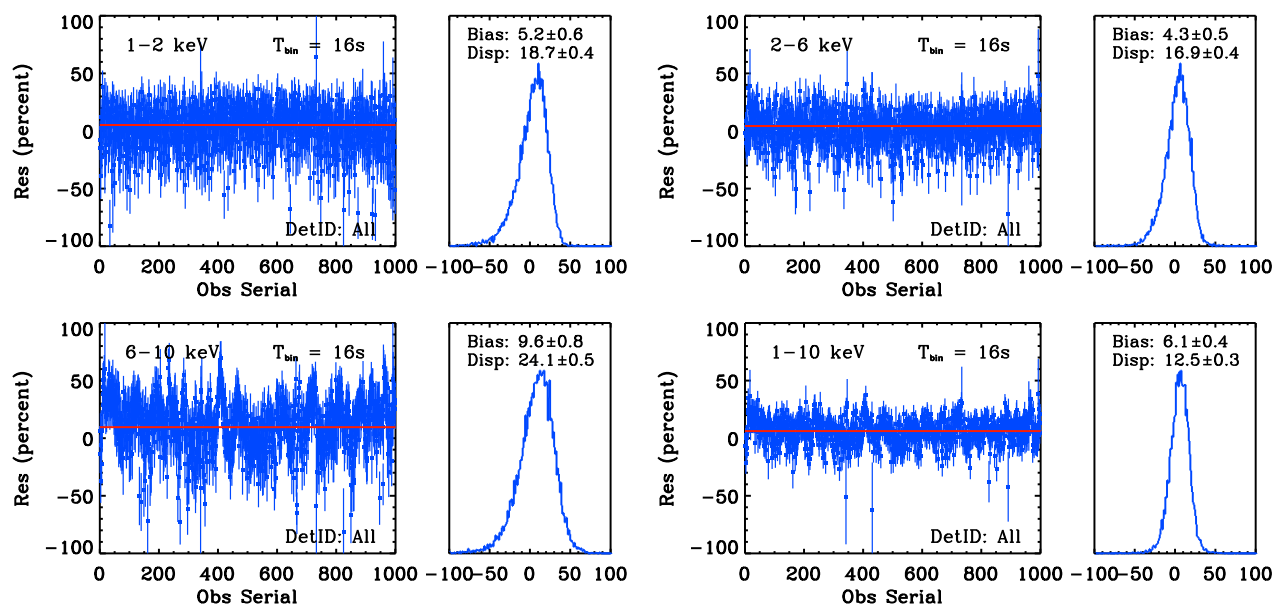


Fig. 17.— Distributions of the residuals in the background estimations of the light curves with $T_{\text{bin}} = 16$ s for four energy bands. In each panel, the broadening of the histogram is the dispersion of the residuals that caused by both the statistical error of the test data and the systematic error of the background model.